Optimal signal-to-noise ratios for soft x-ray lensless imaging

R. Rick,[1,2,*] A. Scherz,[2] W. F. Schlotter,[3] D. Zhu,[1,2] J. Lüning,[4] and J. Stöhr[2]

[1]Department of Applied Physics, Stanford University, 316 Via Pueblo Mall, Stanford, California 94305, USA
[2]Stanford Synchrotron Radiation Lightsource (SSRL), SLAC NAL, Menlo Park, California 94025, USA
[3]Institut für Experimentalphysik, Universität Hamburg, 22761 Hamburg, Germany
[4]Laboratoire de Chimie Physique Matiere et Rayonement, Université Pierre et Marie Curie, 75005 Paris, France
*Corresponding author: rrick@stanford.edu

Received October 13, 2008; revised January 13, 2009; accepted January 13, 2009;
posted January 27, 2009 (Doc. ID 102560); published February 25, 2009

We propose and demonstrate a method to gauge and optimize the signal-to-noise ratios (SNRs) in lensless imaging using partially coherent sources. Through spatial filtering we tuned the coherence width of an incoherent soft x-ray undulator source, and we deduce that there exists an optimal spatial filter setting for imaging micrometer-sized objects, while high-resolution imaging is best executed without spatial filtering. Our SNR analysis, given spatial coherence, allows for an estimation of the required exposure time at synchrotron sources and pulse fluence at x-ray laser sources. © 2009 Optical Society of America

OCIS codes: 030.4280, 110.4980, 260.6048, 340.7430.

Coherent scattering (speckle) x-ray imaging has become widely used because of the increased brightness offered by third-generation synchrotron sources and x-ray lasers [1–4]. In particular, soft x-ray speckle imaging offers micrometer-sized fields of view (FVs) combined with resolutions of a few nanometers. Many absorption edges (C,N,O,K edges, transition metal L edges, rare-earth M edges) allow elemental specificity and higher-scattering cross sections [3,5]. The basic requirement for speckle imaging is sufficient spatial coherence [6]. Conventionally, spatial coherence is measured using a series of Young's double-slit fringe visibilities [7,8]. However, a coded aperture, such as a nonredundant array (NRA), is a more advantageous method to accomplish this task in a single shot [9,10]. Synchrotron undulators emit x rays from uncorrelated bunched electrons, where only each single-electron radiation cone (SERC) is fully coherent. As a result, the spatial coherence width is only a fraction of the total beam width. Through spatial filtering [11], e.g., cutting the SERC divergence, the coherence width is increased in the image of the source at the cost of overall transmission. One can therefore trade photon flux density for spatial coherence, and it is important to know which combination maximizes the speckle signal-to-noise ratio (SNR). In this Letter we address this question for area amplitude interferometers, such as lensless imaging. We use a semiempirical approach, measuring horizontal coherence functions and flux densities in a demagnified image of an undulator source followed by SNR analysis for generic samples positioned in this image.

The experiment was performed at SSRL's coherent scattering beamline 5-2. The undulator's period is $\lambda_u = 6.5$ cm, and the magnetic field strength parameter is $K \approx 0.88$. A 3 GeV electron radiates at wavelength [11] $\lambda = \lambda_u(1 + K^2/2 + \gamma^2\theta^2)/2\gamma^2$, where γ is the ratio of the electron energy to the rest energy and θ is the half angle of the SERC. A grating monochromator selects a photon energy of 924 eV ($\lambda = 1.34$ nm, 80% of the undulator peak intensity) with an energy resolving power of $E/\Delta E \approx 600$. The transmitted SERC has a half angle divergence of $\theta \approx 33$ μrad. Even though bunches of 10^{10} electrons pass through the undulator, the photon degeneracy δ_c [12] of each emerging multielectron radiation pulse is smaller than unity. Hence, the spatial coherence of each pulse is still dominated by the characteristics of each SERC. Projected onto the horizontal plane, the SERC has a probability distribution of $p(\theta_x) = 2/(2\pi\theta \sin[\arccos(\theta_x/\theta)])$ with an rms uncertainty of $\Delta\theta_x = 0.68\theta$, implying a Heisenberg electron position uncertainty or source spatial coherence width of at least $\xi_u \geq \lambda/(4\pi\Delta\theta_x) \approx 5$ μm. A horizontal focusing mirror creates an image of the source at the sample with a magnification factor of $M = 0.37$ [13–15]. The *ab initio* SERC spatial coherence ξ_v at the sample is

$$\xi_v \geq M\frac{\lambda}{(4\pi\Delta\theta_x)} \approx 2\ \mu\text{m}. \quad (1)$$

For sample length scales (LSs) smaller than ξ_v, no spatial filtering is required. The optimal SNR is limited by the maximum photon flux density at the sample. For larger LSs, spatial filtering is used to optimize the SNR by introducing slits at $z_s = 10.8$ m from the undulator. Since the multielectron radiation (MER) has a Gaussian shape with a horizontal width $2\sigma_e \approx 870$ μm $> 2\theta z_s$ and a horizontal angular divergence of $\sigma_e' \approx 43$ μrad $> \theta$, the MER at the slits will be a superposition of many displaced and distorted SERCs. For slit widths $W_s \geq 2\theta z_s \approx 710$ μm, we cut MER and photon flux density in the image, without restricting many SERCs. However, for slit widths $W_s \leq 2\theta z_s \approx 710$ μm, all remaining transmitted SERCs will be cut. We expect the experimental MER spatial coherence width ξ_v' to increase rapidly as the SERC transmission probability is reduced.

We measured the spatial coherence and flux densities for five spatial filter settings by placing an NRA at the sample position and recording their scattering

patterns on a CCD detector. The NRA is an array of apertures, where each aperture pair has a distinct LS, thereby allowing the simultaneous measurement of various spatial coherence function values [16]. The NRA used is shown in Fig. 1(a), allowing interference up to LSs of 23 μm [17]. Its interference patterns are shown in Figs. 1(b) and 1(c) for unfiltered and filtered radiation. Based on Schell's theorem [12], its intensity distribution $I_{\mathrm{CCD}}(q_x) \propto |\mathcal{F}[\mu(\Delta x)A(\Delta x)]|$ is given by a Fourier transform of the NRA autocorrelation, $A(\Delta x)$ and the complex coherence function at the sample, $\mu(\Delta x)$ [18]. We determined $A(\Delta x)$ by sampling one spatial coherence function using a set of double pinhole (DPH) visibilities $|\mu| \approx (I_{\max} - I_{\min})/(I_{\max} + I_{\min})$ as in Figs. 1(d) and 1(e). $A(\Delta x)$ is then given by the deconvolution of the interpolated sampled coherence function from the NRA diffraction pattern. Once $A(\Delta x)$ is known, the spatial filter width W_s can be varied and the spatial coherence functions $|\mu(\Delta x, \xi_v')|$ are deconvolved from the NRA diffraction patterns $I_{\mathrm{CCD}}(q_x, \xi_v')$ as shown in Figs. 2(a) and 2(b). We arbitrarily define the experimental MER spatial coherence width ξ_v' as the full width 70% maximum of our measured spatial coherence functions, since this value is clearly defined for all measured datasets, despite the 23 μm limitation of our NRA. For the unfiltered source, we find $\xi_v' \approx 4$ μm, which is roughly consistent with our *ab initio* rms estimate of $\xi_v \geqslant 2$ μm [19].

The photon flux density at the sample for each spatial filter setting, $\mathrm{d}\Phi_0/\mathrm{d}A(\xi_v')$, was deduced from the integrated photon count rate in the NRA diffraction pattern divided by the transmissive NRA area of 1.8 μm^2. For unfiltered illumination we obtained $\mathrm{d}\Phi_0/\mathrm{d}A \sim 2 \times 10^7$ photons s^{-1} μm^{-2}, consistent with storage ring current and beamline efficiency.

The figure of merit describing the flux-coherence trade-off is the amplitude interferometer SNR. Let us assume for simplicity that there is only a single non-

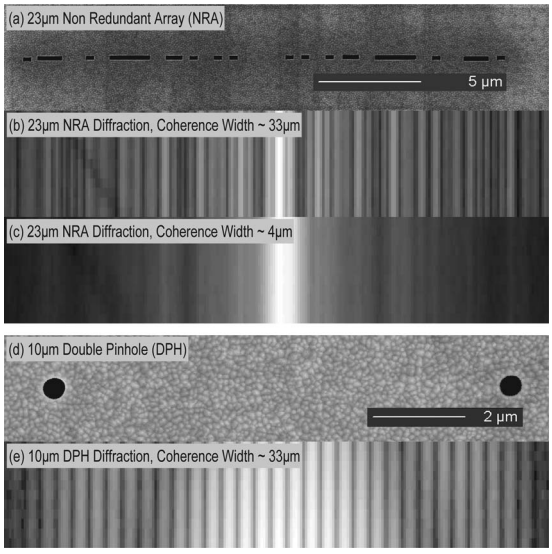

Fig. 1. (a) NRA micrograph [17]. (b) Filtered NRA diffraction ($\lambda = 1.34$ nm). (c) Unfiltered NRA diffraction ($\lambda = 1.34$ nm). (d) DPH micrograph [17]. (e) Filtered DPH diffraction ($\lambda = 1.34$ nm).

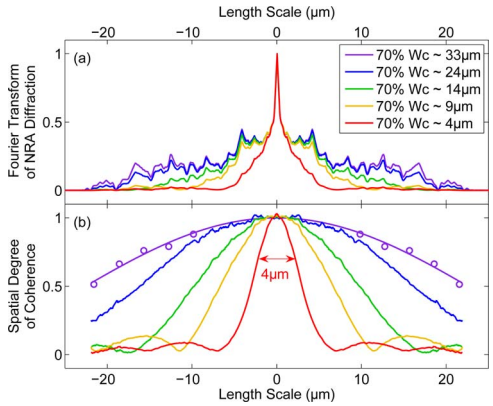

Fig. 2. (a) Fourier transform of NRA diffraction for five different spatial filters. (b) DPH fringe visibilities (circles) interpolate the first spatial coherence function. The remaining coherence functions were deconvolved from their diffraction patterns given the NRA autocorrelation.

periodic LS L to be imaged that is represented by two small scatterers separated by distance L on a transparent background. The fringe visibility SNR is then given by [12]

$$\mathrm{SNR} \approx \frac{|\mu| K}{\sqrt{K}} \approx |\mu| \sqrt{K}, \tag{2}$$

where K is the total photon count. Assuming the typical individual scatterer's size to be a quarter of the distance to its neighbor, the scatterer's effective area is $A \sim \alpha (L/4)^2$, where α is the scattering contrast. The area-integrated photon count during exposure time τ is estimated to be $K \sim (\mathrm{d}\Phi_0/\mathrm{d}A)\alpha(L/4)^2\tau$, using the measured photon flux density $\mathrm{d}\Phi_0/\mathrm{d}A(\xi_v')$.

Given that $|\mu|$ and K ($\alpha = 1$), the SNRs are calculated from Eq. (2) over a range of LSs L, for each of the spatial coherence functions [Fig. 2(b)], and plotted against the coherence width ξ_v' in Fig. 3. The optimal SNR for a single LS is directly given at the coherence width where the SNR is maximal, e.g., the optimum for resolving a 3 μm DPH is $\xi_v' \approx 9$ μm. The

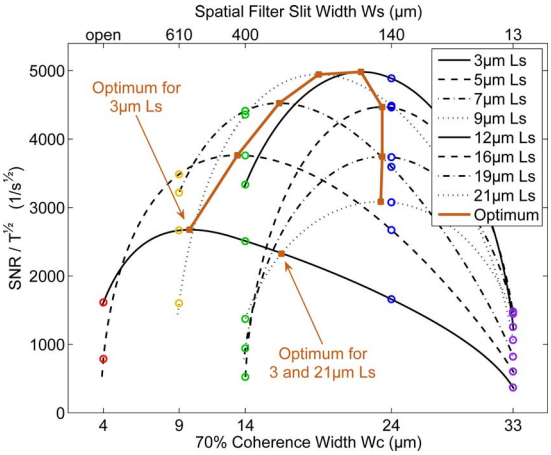

Fig. 3. SNRs for selected LSs as a function of five coherence widths (colored circles). Cubic splines interpolate between them. The optimum curve through the maxima of the splines maps an LS of interest to the spatial coherence width (brown curve and squares).

optimal SNR curve (brown curve) connects between each of these single LS maxima. At short LSs the optimal SNR increases with signal strength ($K \propto L^2$). At longer LSs, the optimal SNR levels off and descends, governed by spatial filtering that cuts the incident photon flux density, $d\Phi_0/dA(\xi_v')$. Finally, beyond 16 μm LSs the optimal SNR declines vertically as it becomes more efficient to exploit the coherence function's first side maximum [Fig. 2(b)] rather than further stretching the central coherence disc.

Since real samples contain many LSs simultaneously with a variety of effective areas and absorption cross sections, a precise SNR analysis would be sample specific. We approximate a generic real sample by a superposition of N displaced double scatterers covering various LSs. For $N=2$ the optimum spatial filter is found, where the minimum of the two SNR curves is maximal as shown in Fig. 3. For $N \gg 1$, e.g., all LSs between 3 and 21 μm, the N SNR curves cannot be considered independently; at the optimal coherence width of 17 μm, the 9 μm LS has the highest signal and the highest noise, therefore the 3 and 21 μm signals need to overcome the 9 μm noise. The resulting SNR can hence be lower, and Fig. 3 provides an upper bound for the realized SNR.

For imaging nanometer sized objects smaller than the unfiltered spatial coherence width, the SNR can be scaled according to $\mathrm{SNR} \propto L\sqrt{\alpha}\sqrt{\tau}$. Scaling an $\mathrm{SNR} \approx 1600\ \mathrm{s}^{-1/2}$ for a 3 μm LS down to 10 nm and assuming a reduced scattering contrast of $\alpha \approx 10\%$, as is common with nanosized samples whose absorption length is larger than their thickness, we expect a high-resolution (HR) SNR on the order of $1.7\ \mathrm{s}^{-1/2}$. However, HR imaging within a larger FV requires that the nanoscale HR signal overcomes the larger FV noise. The relevant SNR becomes [20]

$$\mathrm{SNR} \approx K_{\mathrm{HR}}/\sqrt{K_{\mathrm{FV}}}. \tag{3}$$

Assuming a 100% scattering contrast for LSs of up to 500 nm, the SNR is only $0.01\mathrm{s}^{-1/2}$ for resolving 10 nm features, requiring an estimated 24 h of exposure to reach an SNR around 3. The various LSs involved give insight into why imaging low contrast nanosized objects is superior to imaging large objects with nanosized features or nanosized objects defined by large apertures.

In summary, we have demonstrated an efficient procedure to optimize spatial filtering for amplitude interferometers using incoherent sources, such as soft x-ray synchrotron undulators, and showed optimal imaging conditions for micrometer sized objects. The subsequent simple SNR analysis allows estimation of required x-ray fluences and sheds light on the feasibility of high resolution imaging.

This research was funded by the Office of Basic Energy Sciences, United States Department of Energy (DOE).

References and Notes

1. M. Howells, C. Jacobsen, J. Kirz, R. Feder, K. McQuaid, and S. Rothman, Science **238**, 514 (1987).
2. J. Miao, P. Charalambous, J. Kirz, and D. Sayre, Nature **400**, 342 (1999).
3. S. Eisebitt, J. Lüning, W. F. Schlotter, M. Lörgen, O. Hellwig, W. Eberhardt, and J. Stöhr, Nature **432**, 885 (2004).
4. J. Kirz, Nat. Phys. **2**, 799 (2006).
5. A. Scherz, D. Zhu, R. Rick, W. F. Schlotter, S. Roy, J. Lüning, and J. Stöhr, Phys. Rev. Lett. **101**, 076101 (2008).
6. L. W. Whitehead, G. J. Williams, H. M. Quiney, K. A. Nugent, A. G. Peele, D. Paterson, M. D. de Jonge, and I. McNulty, Phys. Rev. B **77**, 104112 (2008).
7. T. Ditmire, E. T. Gumbrell, R. A. Smith, J. W. G. Tisch, D. D. Meyerhofer, and M. H. R. Hutchinson, Phys. Rev. Lett. **77**, 4756 (1996).
8. K. M. Rosfjord, Y. Liu, and D. Attwood, IEEE J. Sel. Top. Quantum Electron. **10**, 1405 (2004).
9. J. E. Trebes, K. A. Nugent, S. Mrowka, R. A. London, T. W. Barbee, M. R. Carter, J. A. Koch, B. J. MacGowan, D. L. Matthews, L. B. Da Silva, G. F. Stone, and M. D. Feit, Phys. Rev. Lett. **68**, 588 (1992).
10. J. J. A. Lin, D. Paterson, A. G. Peele, P. J. McMahon, C. T. Chantler, K. A. Nugent, B. Lai, N. Moldovan, Z. Cai, D. C. Mancini, and I. McNulty, Phys. Rev. Lett. **90**, 074801 (2003).
11. D. Attwood, *Soft X-Rays and Extreme Ultraviolet Radiation* (Cambridge, 2000).
12. J. W. Goodman, *Statistical Optics* (Wiley, 1985).
13. Van Cittert-Zernike's theorem is inapplicable [14,15].
14. C. Chang, P. Naulleau, and D. Attwood, Appl. Opt. **42**, 14 (2003).
15. G. Geloni, E. Saldin, E. Schneidmiller, and M. Yurkov, Nucl. Instrum. Methods Phys. Res. A **588**, 463 (2008).
16. E. E. Fenimore and T. M. Cannon, Appl. Opt. **17**, 337 (1978).
17. The NRA/DPHs consist of 2 μm gold on a 100 nm silicon nitride membrane, structured with a focused ion beam.
18. We assume a Schell-model source, which by definition is translationally invariant.
19. MER ξ_v' is related to SERC ξ_v by summation of SERCs, lens aberration effects, and a 70% versus rms form factor.
20. This model does not account for diffraction angle (Q) dependent SNRs.